

Iterative Self-consistent Parallel Magnetic Resonance Imaging Reconstruction based on Nonlocal Low-Rank Regularization

Ting Pan, Jizhong Duan, Junfeng Wang, and Yu Liu

Abstract—Iterative self-consistent parallel imaging reconstruction (SPIRiT) is an effective self-calibrated reconstruction model for parallel magnetic resonance imaging (PMRI). The joint L1 norm of wavelet coefficients and joint total variation (TV) regularization terms are incorporated into the SPIRiT model to improve the reconstruction performance. The simultaneous two-directional low-rankness (STDLR) in k-space data is incorporated into SPIRiT to realize improved reconstruction. Recent methods have exploited the nonlocal self-similarity (NSS) of images by imposing nonlocal low-rankness of similar patches to achieve a superior performance. To fully utilize both the NSS in Magnetic resonance (MR) images and calibration consistency in the k-space domain, we propose a nonlocal low-rank (NLR)-SPIRiT model by incorporating NLR regularization into the SPIRiT model. We apply the weighted nuclear norm (WNN) as a surrogate of the rank and employ the Nash equilibrium (NE) formulation and alternating direction method of multipliers (ADMM) to efficiently solve the NLR-SPIRiT model. The experimental results demonstrate the superior performance of NLR-SPIRiT over the state-of-the-art methods via three objective metrics and visual comparison.

Index Terms—iterative self-consistent parallel imaging reconstruction (SPIRiT), nonlocal low-rank (NLR), Nash equilibrium (NE), parallel magnetic resonance imaging (PMRI), compressed sensing (CS), alternating direction method of multipliers (ADMM), weighted nuclear norm (WNN)

I. INTRODUCTION

Magnetic resonance (MR) imaging (MRI) provides an indispensable imaging method without ionizing radiation in contemporary clinical applications. However, the scanning speed of MR imaging technique is limited. Both compressed sensing (CS) and parallel imaging (PI) techniques have been applied to reduce the MRI scanning time.

A variety of k-space undersampling patterns has been applied to reduce the amount of collected data, such as one-dimensional (1D) uniform undersampling (1DUU), 1D Gaussian random undersampling (1DGU), two-dimensional (2D) Poisson-disc undersampling (2DPU), 2D Gaussian random

undersampling (2DGU), and radial undersampling. According to the CS theory [1], [2], it is feasible to reconstruct the MR images from highly undersampled measurements [2], since the MR images exhibit a sparsity in the wavelet transform domain and spatial finite differences. CS-MRI methods [2], [3] have been proposed to solve reconstruction problems with regularization terms of the total variation (TV) and L1 norm of wavelet coefficients. Qu et al. developed the patch-based directional wavelet (PBDW and PBDWS) [4], [5] and graph-based redundant wavelet transform (GBRWT) [6] to improve the reconstruction performance. In addition to fixed sparse transform methods, adaptive sparse representation-based reconstruction methods have been proposed, such as dictionary learning-based MRI (DLMRI) [7] and transform learning-based MRI (TLMRI) [8]–[11] algorithms. These algorithms have been proven to attain a high reconstruction performance.

Certain methods have been proposed to exploit the nonlocal self-similarity (NSS) of image patches to improve the image quality, such as the nonlocal means (NL-means) [12], block-matching 3D denoising (BM3D) [13], [14], patch-based nonlocal operator (PANO) [15], and nonlocal low-rank (NLR)-CS [16] methods. The BM3D method exploits the NSS of image patches via their grouping for image denoising purposes [13], [14], which has been applied in MRI reconstruction. Qu et al. [15] exploited the NSS of image patches and established a PANO to reduce the reconstruction error. Dong et al. [16] developed the very promising NLR-CS model employing NLR regularization of similar image patches constructed through block matching (BM).

Parallel MRI (PMRI) is also a well-known technique to accelerate MRI, which is often combined with the CS theory to improve the reconstruction performance. Sensitivity encoding (SENSE) [17] explicitly utilizes sensitivity information. However, the performance of these methods is limited due to the difficulty in the accurate measurement of sensitivity information in practical applications. An iterative self-consistent parallel imaging reconstruction using eigenvector maps (ESPIRiT) model has been proposed [18]. In contrast to the SENSE model, ESPIRiT model estimates multiple sets of coil sensitivity. We [19] introduced the Lp pseudo-norm joint TV regularization term into the ESPIRiT scheme to improve the reconstruction performance.

Another type of PMRI reconstruction method avoids the difficulty in sensitivity estimation by implicitly considering sensitivity information, such as the generalized autocalibrating partially parallel acquisitions (GRAPPA) [20], [21] and itera-

This work was supported in part by the National Natural Science Foundation of China under Grant 61861023, Yunnan key research program (2018IB007), and Medical leading talents Project in Yunnan Province (L-2019016).

T. Pan is with the Faculty of Information Engineering and Automation, Kunming University of Science and Technology, Kunming 650500, China.

J. Duan is with the Faculty of Information Engineering and Automation, Kunming University of Science and Technology, Kunming 650500, China. (e-mail: duanjz@kust.edu.cn). *Corresponding Author.*

J. Wang is with the Department of Hepatobiliary Surgery, The First People's Hospital of Yunnan Province, Kunming 650030, China.

Y. Liu is with the School of Microelectronics, Tianjin University, Tianjin 300072, China.

tive self-consistent parallel imaging reconstruction (SPIRiT) [22]–[27] methods, which relies on the k-space local kernel calibration. SPIRiT includes two reconstruction schemes in both the image [23], [24], [26] and k-space [22], [23], [25] domains. An L1-SPIRiT scheme has been obtained by combining the regularization term of the joint L1 norm (JL1) in the wavelet domain with the k-space domain-based SPIRiT model and solved with the projection over convex sets (POCS) algorithm [22], [25]. Duan *et al.* [27] applied the fast iterative shrinkage thresholding algorithm (FISTA) to solve the SPIRiT PMRI reconstruction problem in the k-space domain with the joint TV (JTV) regularization term. Weller *et al.* [26] adopted the alternating direction method of multipliers (ADMM) technique to solve the SPIRiT PMRI reconstruction problem in the image domain with the JTV regularization term. Most recently, the STDLR-SPIRiT scheme has been established [28] by combining the SPIRiT model with the simultaneous two-directional low-rankness (STDLR) in k-space to realize improved reconstruction. In fact, STDLR-SPIRiT has exploited the local low-rank (LR) prior rather than the LR feature based on nonlocal image structures.

Recent methods have exploited the NSS of images by imposing the group sparsity or the low-rankness of nonlocal similar patches to improve the reconstruction quality. Among them, the NLR-based methods have achieved an excellent performance [16], [29]. In addition, there have been a variety of improved SPIRiT-based methods for PMRI reconstruction. However, to the best of our knowledge, no SPIRiT-based algorithm has applied low-rankness of nonlocal similar patches. In this paper, we propose an NLR-SPIRiT scheme incorporating NLR regularization into the SPIRiT model. The NLR-SPIRiT model fully utilizes both the NSS in MR images and the calibration consistency in the k-space domain to improve the reconstruction performance. By employing the Nash equilibrium (NE) formulation [30], [31], we reformulate the NLR-SPIRiT model into a two-objective optimization problem including a rank minimization problem and a least-squares (LS) problem. We adopt the weighted nuclear norm (WNN) instead of the nuclear norm (NN) as a surrogate of the rank, which yields a more efficient method to solve the rank minimization problem. The LS problem is efficiently solved with the ADMM technique. The experimental results demonstrate the superior performance of the NLR-SPIRiT model over state-of-the-art methods in terms of three objective metrics and visual comparison.

We organize the rest of this article as follows: in Section II, we review the SPIRiT model and SPIRiT-based algorithms. In Section III, we describe the NLR-SPIRiT model, which incorporates NLR regularization of similar patches into the SPIRiT model. We adopt the WNN as a surrogate of the rank and employ the NE formulation and ADMM technique to efficiently solve the NLR-SPIRiT model. Section IV presents the experimental results and analysis. Finally, we provide the conclusion of this paper in Section V.

II. RELATED WORK

Suppose $X \in \mathbb{C}^{NC}$ represents a multicoil image stacked in columns, $Y \in \mathbb{C}^{MC}$ denotes the undersampled k-space data

of the multicoil image stacked in columns, $P \in \mathbb{R}^{M \times N}$ is an undersampled operator selecting only the acquired k-space data from the entire k-space grid, $U \in \mathbb{C}^{N_x \times N_y}$ is the discrete 2D Fourier transform matrix, $F = U \otimes U \in \mathbb{C}^{N \times N}$ is the Fourier operator applied on single coil image, $\mathcal{F} = I_C \otimes F \in \mathbb{C}^{NC \times NC}$, $\mathcal{P} = I_C \otimes P \in \mathbb{C}^{MC \times NC}$, $\mathcal{A} = \mathcal{P}\mathcal{F} \in \mathbb{C}^{MC \times NC}$ represents the undersampled encoding matrix, I_C is a $C \times C$ identity matrix, \otimes denotes Kronecker product, $N = N_x \times N_y$, and C is the total number of coils. The undersampled k-space data of multicoil images are thus given by:

$$Y = AX \quad (1)$$

The SPIRiT calibration consistency equation in the image domain is expressed as:

$$X = GX \quad (2)$$

where G is the image domain-based SPIRiT operator, acquired from autocalibration signal (ACS) lines (as shown in Fig. 1(a)).

Murphy *et al.* [24] proposed the image domain-based L1-SPIRiT model by introducing the joint sparsity to improve the reconstruction quality. The image domain-based L1-SPIRiT minimization problem is as follows:

$$\arg \min_X \|\Psi X\|_{2,1} \quad s.t. \quad Y = AX, \quad GX = X \quad (3)$$

where Ψ is the coil-by-coil wavelet transform, and $\|\cdot\|_{2,1}$ denotes joint L1 norm. A simple and efficient POCS algorithm is developed to solve problem (3).

The JL1 and JTV regularization terms are [26] combined with the image domain-based SPIRiT model, and the corresponding optimization problem is given by:

$$\arg \min_X \|AX - Y\|_F^2 + \mu \|(G - I)X\|_F^2 + \tau_1 \|\Psi X\|_{2,1} + \tau_2 \|X\|_{\text{JTV}} \quad (4)$$

where $\|\cdot\|_{\text{JTV}}$ denotes the JTV regularization term. The above optimization problem (4) can be solved with the ADMM technique.

Next, we introduce the k-space domain-based SPIRiT model. The SPIRiT calibration consistency equation in the k-space domain is expressed as:

$$S = \tilde{G}S \quad (5)$$

where $S = \mathcal{F}X$ denotes the k-space data of the multicoil image X , and \tilde{G} is the k-space domain SPIRiT operator, which convolves a series of calibration kernels acquired from the ACS lines with the entire k-space.

The undersampled k-space data of multicoil images are determined as:

$$Y = \mathcal{P}S \quad (6)$$

Vasanawala *et al.* proposed the k-space-based L1-SPIRiT model by introducing the joint sparsity to enhance the reconstruction quality [22]. The L1-SPIRiT model in k-space can be expressed as the following minimization problem:

$$\arg \min_S \|\Psi \mathcal{F}^{-1}S\|_{2,1} \quad s.t. \quad Y = \mathcal{P}S, \quad S = \tilde{G}S \quad (7)$$

Problem (7) is solved with the POCS algorithm [22]. We also discussed the solution to problem (7), and proposed

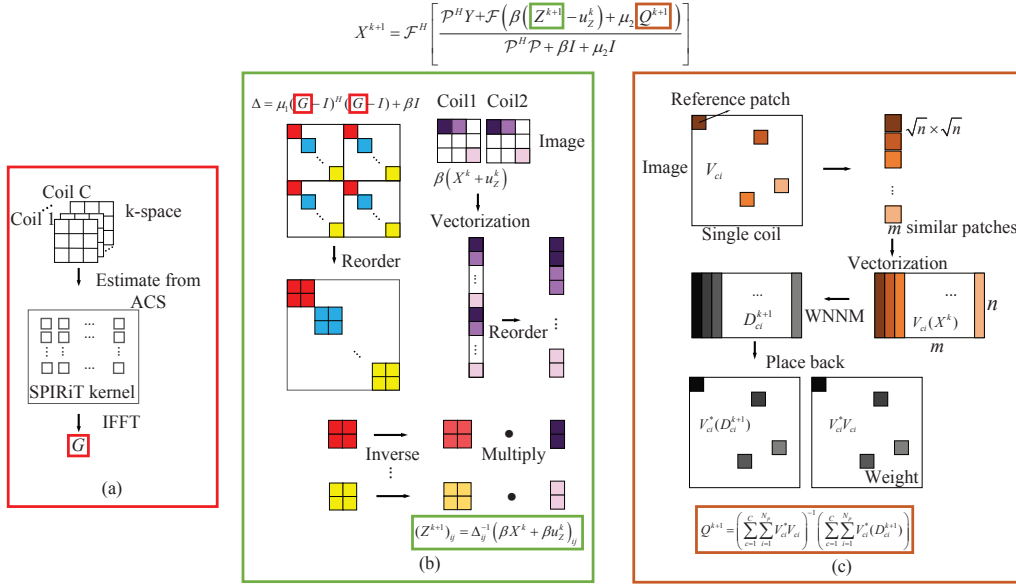


Fig. 1. The schematic illustration of NLR-SPIRiT. (a) Calculation of G : A series of SPIRiT kernels are estimated through k-space autocalibration signal (ACS). The matrix G is obtained by calculating the IFFT of the matrix composed of SPIRiT kernels. (b) Preprocessing steps for calculating (take only two coils as an example): The matrix $\Delta = \mu_1(G - I)^H(G - I) + \beta I$ has a diagonal-block structure, then a simple reordering of the matrix yields a block-diagonal structure. The inverse of the matrix, Δ^{-1} , is computed by directly inverting each block. (c) Non-local low-rank denoising: Choose similar patches closest to the reference patch in terms of the Euclidean distance. The selected similar patches are vectorized and grouped to construct a similar patch group matrix $V_{ci}(X)$. The low-rank approximation D_{ci} is obtained by solving the weighted nuclear norm minimization (WNNM) problem, and then placed back to the original positions.

an algorithm with a higher reconstruction quality than that obtained with the POCS algorithm [25].

We introduce the JTV regularization term into the k-space-based SPIRiT model to increase the reconstruction quality [27], and the corresponding optimization problem is given by:

$$\arg \min_S \lambda_1 \| \mathcal{P}S - Y \|_F^2 + \lambda_2 \left\| \left(\tilde{G} - I \right) S \right\|_F^2 + \gamma_1 \left\| \Psi \mathcal{F}^{-1} S \right\|_{2,1} + \gamma_2 \left\| \mathcal{F}^{-1} S \right\|_{\text{JTV}} \quad (8)$$

The FISTA and ADMM techniques are applied to solve problem (8) [27].

By combining the k-space-based SPIRiT model with the STDLR regularization term, Zhang et al. proposed the following STDLR-SPIRiT model [28]:

$$\arg \min_S \frac{\lambda_1}{2} \| \mathcal{P}S - Y \|_F^2 + \frac{\lambda_2}{2} \left\| \left(\tilde{G} - I \right) S \right\|_F^2 + \left\| \tilde{\mathcal{H}} \mathcal{W}_= S \right\|_* + \left\| \tilde{\mathcal{H}} \mathcal{W}_\perp S \right\|_* \quad (9)$$

where $\tilde{\mathcal{H}} \mathcal{W}_= S = [HW_= \odot S_1, \dots, HW_= \odot S_c, \dots, HW_= \odot S_C]$ is a fatter matrix comprising stacked Hankel matrices in the horizontal direction, $\tilde{\mathcal{H}} \mathcal{W}_\perp S = [HW_\perp \odot S_1, \dots, HW_\perp \odot S_c, \dots, HW_\perp \odot S_C]$ is a fatter matrix comprising stacked Hankel matrices in the vertical direction, \odot is the Hadamard product, H is an operator to convert S into a block Hankel matrix, and W_\perp and $W_=$ are the weights corresponding to the Fourier transform coefficients of sparse transform filters in the vertical and horizontal directions, respectively. Problem (9) can be solved with the ADMM technique.

III. THE PROPOSED ALGORITHM

A. Problem formulation

Past works have verified that the NSS prior information facilitated sparsity enforcement, resulting in reconstruction quality enhancement. To further improve the PMRI reconstruction quality, we incorporate the NLR regularization term into the SPIRiT model to fully utilize the NSS of PMRI.

Suppose $X_c \in \mathbb{C}^N$ denotes the c^{th} coil image of X , and a single coil image is divided into N_p overlapping patches of size $\sqrt{n} \times \sqrt{n}$. In each reference patch, we search for similar patches within a local window (e.g., 40×40), and choose m similar patches closest to the reference patch in terms of the Euclidean distance. The selected similar patches are vectorized and grouped to construct a similar patch group matrix $V_{ci}(X) \in \mathbb{C}^{n \times m}$, where $V_{ci}: X \in \mathbb{C}^{N \times C} \mapsto V_{ci}(X) \in \mathbb{C}^{n \times m}$ is a BM operator. The step of obtaining NSS prior information is depicted in Fig. 1(c). Therefore, the PMRI reconstruction problem based on the NLR regularization term and the SPIRiT model can be formulated as the following problem:

$$X = \arg \min_X \frac{1}{2} \| AX - Y \|_F^2 + \frac{\mu_1}{2} \| (G - I)X \|_F^2 + \tau \sum_{c=1}^C \sum_{i=1}^{N_p} \text{rank}(V_{ci}(X)) \quad (10)$$

where $\text{rank}(V_{ci}(X))$ denotes the rank of the matrix $V_{ci}(X)$, μ_1 and τ are tuning parameters, which are applied to balance the data fidelity, the calibration consistency, and the NLR regularization term.

B. Problem solution

Problem (10) is a large-scale nonconvex optimization problem that is difficult to solve. Authors [30], [31] have proposed employing an NE formulation. With the application of the NE formulation [30], [31], we convert the reconstruction (10) into a two-objective optimization problem:

$$\{D_{ci}^{k+1}\} = \arg \min_{\{D_{ci}\}} \frac{1}{2} \|V_{ci}(X^k) - D_{ci}\|_F^2 + \tau \text{rank}(D_{ci}) \quad (11)$$

$$X^{k+1} = \arg \min_X \|AX - Y\|_F^2 + \mu_1 \|(G - I)X\|_F^2 + \mu_2 \|X - Q^{k+1}\|_F^2 \quad (12)$$

where D_{ci}^{k+1} denotes LR approximation of the patch group matrix $V_{ci}(X^k)$, and Q^{k+1} is determined as follows:

$$Q^{k+1} = \left(\sum_{c=1}^C \sum_{i=1}^{N_p} V_{ci}^* V_{ci} \right)^{-1} \left(\sum_{c=1}^C \sum_{i=1}^{N_p} V_{ci}^* (D_{ci}^{k+1}) \right) \in \mathbb{C}^{NC} \quad (13)$$

where $V_{ci}^* : \mathbb{C}^{n \times m} \mapsto \mathbb{C}^{NC}$, the adjoint operator of V_{ci} , places back the denoised patches D_{ci}^{k+1} at their original positions (as shown in Fig. 1(c)). $\sum_{c=1}^C \sum_{i=1}^{N_p} V_{ci}^* V_{ci} \in \mathbb{C}^{NC \times NC}$ is a diagonal matrix with each diagonal element equal to the time of the corresponding pixel belonging to the overlapping patches throughout $\{V_{ci}(X)\}$.

1) *Minimization with respect to $\{D_{ci}\}$* : Generally, the rank penalty objective optimization problem of $\{D_{ci}\}$ is a non-deterministic polynomial time (NP)-hard problem. Thus, given that the WNN [32], [33] may yield a better rank approximation than the NN, we adopt the WNN as a convex surrogate of the rank. The WNN of $\{D_{ci}\}$ can be written as:

$$\|D_{ci}\|_{w,*} = \sum_{j=1}^{\min(n,m)} w_j \sigma_j(D_{ci}) \quad (14)$$

With the use of the WNN as a surrogate of the rank, let $2\tau = \delta^2$, problem (11) can be rewritten as follows:

$$\{D_{ci}^{k+1}\} = \arg \min_{\{D_{ci}\}} \|V_{ci}(X^k) - D_{ci}\|_F^2 + \delta^2 \|D_{ci}\|_{w,*} \quad (15)$$

Problem (15) is a weighted nuclear norm minimization (WNNM) [32] problem. Let $U\Sigma V^H = V_{ci}(X^k)$ be the full singular value decomposition (SVD) of $V_{ci}(X^k)$, $\Sigma = \text{diag}(\sigma_1(V_{ci}(X^k)), \dots, \sigma_j(V_{ci}(X^k)), \dots, \sigma_J(V_{ci}(X^k)))$, $\sigma_j(V_{ci}(X^k))$ is the j^{th} singular value of $V_{ci}(X^k)$, and $J = \min(m, n)$. Hence, the optimal solution to (15) is $D_{ci}^{k+1} = U\Gamma V^T$, $\Gamma = \text{diag}(\gamma_1, \dots, \gamma_j, \dots, \gamma_J)$, where γ_j can be calculated as:

$$\gamma_j = \text{soft}(\sigma_j(V_{ci}(X^k)), w_j) \quad (16)$$

where $\text{soft}(\cdot)$ is the soft threshold operator, $\text{soft}(\sigma, w) = \max(\sigma - w, 0)$. And the weight w_j can be calculated as:

$$w_j = \frac{b_0 \sqrt{m}}{\hat{\sigma}_j + \varepsilon} \quad (17)$$

where b_0 is a constant, $\varepsilon = 10^{-16}$ is to avoid dividing by zero, and then the initial $\hat{\sigma}_j$ can be estimated as:

Algorithm 1 NLR regularization-based SPIRiT (NLR-SPIRiT) PMRI reconstruction algorithm

-
- 1: Input: undersampled k-space data Y of the multicoil image.
 - 2: Set $X^0 = F^{-1}Y$, $Z^0 = 0$, $u_Z^0 = 0$, $k = 0$, $\Delta^{-1} = (\mu_1(G - I)^H(G - I) + \beta I)^{-1}$
 - 3: **repeat**
 - 4: If $\text{mod}(k, T) = 0$, update the patch grouping V_{ci} by BM.
 - 5: Construct similar patch group matrix $V_{ci}(X^k)$.
 - 6: **for** each group $V_{ci}(X^k)$ **do**
 - 7: Compute the full SVD of $U\Sigma V^T$ of $V_{ci}(X^k)$.
 - 8: Update the weights w_j via Eq. (17).
 - 9: Compute $\Gamma = \text{diag}(\gamma_1, \dots, \gamma_j, \dots, \gamma_J)$, where γ_j was computed via Eq. (16).
 - 10: Compute $D_{ci}^{k+1} = U\Gamma V^T$.
 - 11: **end for**
 - 12: Compute Q^{k+1} via Eq. (13).
 - 13: Compute $Z^{k+1} = \Delta^{-1}(\beta X^k + \beta u_Z^k)$.
 - 14: Compute X^{k+1} via Eq. (23).
 - 15: Update u_Z^{k+1} via Eq. (21).
 - 16: Compute x^{k+1} via Eq. (24).
 - 17: $k = k + 1$.
 - 18: **until** $RE < \text{tol}$
 - 19: Output the reconstructed image \hat{X} .
-

$$\hat{\sigma}_j = \sqrt{\max(\sigma_j(V_{ci}(X^k))^2 - m\delta^2, 0)} \quad (18)$$

2) *Image reconstruction*: After calculating $\{D_{ci}^{k+1}\}$, the whole image can be reconstructed by solving problem (12). By introducing an auxiliary variable $Z = X$ and corresponding Lagrange multiplier u_Z , the LS problem (12) can be converted to the following subproblems via the ADMM technique:

$$Z^{k+1} = \arg \min_Z \mu_1 \|(G - I)Z\|_F^2 + \beta \|Z - (X^k + u_Z^k)\|_F^2 \quad (19)$$

$$X^{k+1} = \arg \min_X \|AX - Y\|_F^2 + \beta \|X - Z^{k+1} + u_Z^k\|_F^2 + \mu_2 \|X - Q^{k+1}\|_F^2 \quad (20)$$

$$u_Z^{k+1} = u_Z^k + \eta (X^{k+1} - Z^{k+1}) \quad (21)$$

The solution to subproblem (19) with respect to Z is given by:

$$Z^{k+1} = \left[\mu_1(G - I)^H(G - I) + \beta I \right]^{-1} (\beta X^k + \beta u_Z^k) \quad (22)$$

Let $\Delta = \mu_1(G - I)^H(G - I) + \beta I$, and Δ^{-1} can thus be obtained via the direct inversion of each $C \times C$ block in matrix Δ , as shown in Fig. 1(b). Then, we have the update of Z as $Z^{k+1} = \Delta^{-1}(\beta X^k + \beta u_Z^k)$. $\mathcal{P}^H \mathcal{P}$ is a diagonal matrix, and subproblem (20) with respect to X yields the following closed-form solution:

$$X^{k+1} = \mathcal{F}^H \left[\frac{\mathcal{P}^H Y + \mathcal{F}(\beta(Z^{k+1} - u_Z^k) + \mu_2 Q^{k+1})}{\mathcal{P}^H \mathcal{P} + \beta I + \mu_2 I} \right] \quad (23)$$

Since subproblems (11), (19), and (20) are efficiently solved, the C-coil image X is obtained, and then combined

into a single magnitude image x by using the square root of sum of squares (SOS):

$$x = \text{SOS}(X) = \sqrt{\sum_{c=1}^C |X_c|^2} \quad (24)$$

Finally, we obtain the NLR regularization-based SPIRiT (NLR-SPIRiT) PMRI reconstruction algorithm, as expressed in Algorithm 1. And the schematic illustration of NLR-SPIRiT is described in Fig. 1. Algorithm 1 is terminated when the relative error (RE) $RE = \frac{\|x^{k+1} - x^k\|_2}{\|x^k\|_2}$ falls below the tolerance tol . In Algorithm 1, the BM step is performed every T iterations to reduce the computational complexity, as shown in step 4.

The optimization problem (10) can also be solved by using the variable splitting and ADMM techniques. The corresponding algorithm is called ADMM-NLR-SPIRiT. Please refer to the appendix for details.

IV. EXPERIMENTAL RESULTS

A. Experimental setup

In our experiments, we compared the proposed NLR-SPIRiT model to state-of-the-art algorithms to solve the PMRI reconstruction problems such as: JTV-SPIRiT [26], LPJTV-ESPIRiT [19], STDLR-SPIRiT [28], and NLR-SPIRiT-baseline (a variant of the NLR-SPIRiT model with the standard NN). All the considered algorithms were implemented in MATLAB.

To validate the performances of all the considered algorithms, we conduct experiments on four fully sampled in vivo human datasets. The first fully sampled brain dataset [34] (dataset 1, as shown in Fig. 3(a)) was acquired on a clinical MR scanner Discovery MR750 using a 12-channel head-neck spine coil and a 3D T1-weighted gradient echo sequence (matrix size = $256 \times 218 \times 170$, TR/TE = 7.4/3.1 ms, field of view (FOV) = $256 \times 218 \times 170$ mm, slice thickness = 1 mm). We chose a single slice of each multislice dataset in our experiment. The second fully sampled knee dataset [35] (dataset 2, as shown in Fig. 4(a)) was acquired on a GE scanner using an 8-channel HD knee coil and a 3D FSE CUBE sequence (matrix size = $320 \times 320 \times 256$, TR/TE = 1550/25 ms, FOV = 160×160 mm, slice thickness = 0.6 mm). We chose a single slice of each multislice dataset in our experiment. The third fully sampled brain dataset [36] (dataset 3, as shown in Fig. 5(a)) was acquired on a 3T SIEMENS Trio system and an 8-channel head array coil (matrix size = 256×256 , TR/TE = 2530/3.45 ms, slice thickness = 1.33 mm, FOV = 256×256 mm). The fourth fully sampled brain dataset [28] (dataset 4, as shown in Fig. 6(a)) was acquired on a 3T SIEMENS Trio whole-body scanner using a 32-coil head coil and the 2D T2-weighted turbo spin echo sequence (matrix size = 256×256 , TR/TE = 6100/99 ms, FOV = 220×220 mm, slice thickness = 3 mm). The 32-channel k-space data was compressed to four virtual coils.

To validate the considered algorithms, fully sampled datasets were subjected to retrospective undersampling with the above different undersampling patterns and acceleration

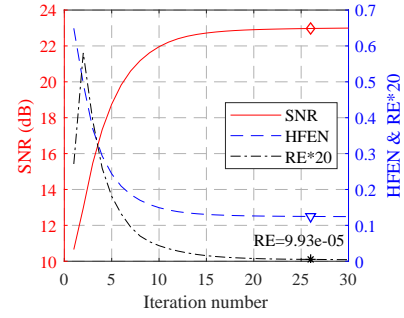


Fig. 2. SNR, HFEN and RE versus the iteration number when reconstructing the dataset 1 based on the 2DPU pattern ($AF = 5$).

factors (AFs) (including ACS lines). In our experiments, we employed two undersampling patterns, 2DPU and 1DPU. It should be noted that the 2DPU patterns always include 24×24 ACS lines, and the 1DPU pattern includes 20 ACS lines. All experiments were simulated on a workstation machine equipped with an Intel Core i9-10900X @ 3.7 GHz processor, 64 G of RAM memory and a Windows 10 operating system (64 bit).

Three commonly adopted objective metrics were employed to evaluate the quality of the reconstructed images, namely, the signal-to-noise ratio (SNR) [27], high-frequency error norm (HFEN) [7], and structural similarity index measure (SSIM) [37]. It should be noted that the calculation of all metrics is limited to the region of interest (ROI). High SNR and SSIM values or low HFEN values indicate more accurate reconstruction. In regard to reference image x and the reconstructed image \hat{x} , the SNR is defined as:

$$SNR = 10 \log_{10} \left(\frac{Var}{MSE} \right) \quad (25)$$

where MSE denotes the mean square error between x and \hat{x} , and Var is the variance in x .

The HFEN is expressed as:

$$HFEN = \frac{\|filter(\hat{x}) - filter(x)\|_2}{\|filter(x)\|_2} \quad (26)$$

where $filter(\cdot)$ is a Laplacian Gaussian filter operator used to determine the image edges.

The SSIM is calculated as:

$$SSIM = \frac{(2u_x u_{\hat{x}} + c_1)(2\sigma_{x\hat{x}} + c_2)}{(u_x^2 + u_{\hat{x}}^2 + c_1)(\sigma_x^2 + \sigma_{\hat{x}}^2 + c_1)} \quad (27)$$

where u_x and $u_{\hat{x}}$ are the means of x and \hat{x} , respectively, σ_x^2 and $\sigma_{\hat{x}}^2$ are the variances of x and \hat{x} , respectively, $\sigma_{x\hat{x}}$ represents the covariance of x and \hat{x} , c_1 and c_2 are constant.

B. Parameter settings

A kernel size of 5×5 was adopted in the SPIRiT-based algorithms in the following experiments. The parameters of JTV-SPIRiT, LPJTV-ESPIRiT, and STDLR-SPIRiT were manually tuned for SNR optimal. In regard to NLR-SPIRiT-baseline and NLR-SPIRiT, 6×6 ($n = 36$) image patches were used, and the total number of similar patches was 43 ($m = 43$). A reference image patch was extracted every 5 pixels along the horizontal and vertical directions to reduce the computational complexity.

TABLE I

COMPARISON OF THE THREE METRICS OF THE RECONSTRUCTED IMAGES VIA THE COMPETING ALGORITHMS BASED ON 2DPU PATTERNS ($AF = 3 - 7$) FOR DATASET 1.

Algorithms	Metrics	Acceleration Factor (AF)				
		3	4	5	6	7
JTV-SPIRiT [26]	SNR	24.35	22.85	21.55	20.38	19.56
	HFEN	0.0938	0.1197	0.1505	0.1816	0.2048
	SSIM	0.9679	0.9585	0.9483	0.9373	0.9277
LPJTV-ESPIRiT [19]	SNR	24.24	22.73	21.50	20.33	19.53
	HFEN	0.0942	0.1203	0.1479	0.1802	0.2008
	SSIM	0.9696	0.9593	0.9341	0.9363	0.9264
STDLR-SPIRiT [28]	SNR	24.54	22.91	21.45	20.22	19.34
	HFEN	0.0898	0.1141	0.1438	0.1715	0.1943
	SSIM	0.9689	0.9577	0.9452	0.9328	0.9220
NLR-SPIRiT-baseline	SNR	24.79	23.37	22.16	21.16	20.36
	HFEN	0.0898	0.1122	0.1381	0.1605	0.1804
	SSIM	0.9712	0.9626	0.9532	0.9436	0.9344
NLR-SPIRiT	SNR	25.37	24.16	22.91	21.90	21.05
	HFEN	0.0810	0.0995	0.1244	0.1509	0.1744
	SSIM	0.9749	0.9690	0.9612	0.9516	0.9429

TABLE II

COMPARISON OF THE THREE METRICS OF THE RECONSTRUCTED IMAGES VIA THE COMPETING ALGORITHMS BASED ON 2DPU PATTERNS ($AF = 3 - 7$) FOR DATASET 2.

Algorithms	Metrics	Acceleration Factor (AF)				
		3	4	5	6	7
JTV-SPIRiT [26]	SNR	18.75	17.53	16.85	16.23	15.76
	HFEN	0.2507	0.3022	0.3272	0.3568	0.3855
	SSIM	0.9161	0.8953	0.8831	0.8739	0.8638
LPJTV-ESPIRiT [19]	SNR	19.20	17.97	17.41	16.75	16.20
	HFEN	0.2110	0.2552	0.2801	0.3062	0.3349
	SSIM	0.9233	0.9014	0.8307	0.8781	0.8663
STDLR-SPIRiT [28]	SNR	19.34	17.83	17.02	16.07	15.24
	HFEN	0.2245	0.2810	0.3084	0.3483	0.3886
	SSIM	0.9262	0.9026	0.8878	0.8714	0.8524
NLR-SPIRiT-baseline	SNR	19.13	18.42	17.75	17.20	16.67
	HFEN	0.2146	0.2427	0.2655	0.2909	0.3143
	SSIM	0.9201	0.9094	0.8984	0.8889	0.8781
NLR-SPIRiT	SNR	20.24	19.08	18.33	17.75	17.19
	HFEN	0.1860	0.2184	0.2421	0.2667	0.2921
	SSIM	0.9352	0.9172	0.9049	0.8947	0.8852

The main parameters were defined as follows: $\mu_1 = \mu_2 = 1$, $b_0 = 0.4$, and $\eta = \sqrt{2}$. These settings remained fixed in all experiments.

In addition, to obtain a better parallel image reconstruction performance, the parameter δ and β were adjusted to optimize the SNR and HFEN values. We run the proposed algorithm on the same undersampled data considering the ranges of $\delta \in [1, 6]$ and $\beta \in [0.1, 1]$. We chose δ and β based on the highest SNR and smallest HFEN values. For example, at $\delta = 3$ and $\beta = 0.3$, these two optimal indicators (SNR and HFEN) of dataset 1 were roughly optimized.

C. Convergence analysis

To reflect the convergence of the proposed NLR-SPIRiT algorithm, Fig. 2 shows SNR, HFEN, and RE versus the iteration number during the reconstruction of dataset 1 based on the 2DPU pattern ($AF = 5$). We observe that NLR-SPIRiT

TABLE III

COMPARISON OF THE THREE METRICS OF THE RECONSTRUCTED IMAGES VIA THE COMPETING ALGORITHMS BASED ON 2DPU PATTERNS ($AF = 3 - 7$) FOR DATASET 3.

Algorithms	Metrics	Acceleration Factor (AF)				
		3	4	5	6	7
JTV-SPIRiT [26]	SNR	27.36	24.73	22.65	20.55	19.22
	HFEN	0.1362	0.1836	0.2322	0.2994	0.3382
	SSIM	0.9756	0.9619	0.9463	0.9273	0.9112
LPJTV-ESPIRiT [19]	SNR	27.46	25.06	23.11	21.22	20.02
	HFEN	0.1322	0.1734	0.2162	0.2743	0.3096
	SSIM	0.9810	0.9704	0.9585	0.943	0.9291
STDLR-SPIRiT [28]	SNR	27.53	25.11	22.99	20.94	19.48
	HFEN	0.1333	0.1765	0.2245	0.2882	0.3316
	SSIM	0.9807	0.9702	0.9576	0.9409	0.9250
NLR-SPIRiT-baseline	SNR	27.74	25.36	23.80	21.80	20.45
	HFEN	0.1294	0.1685	0.2022	0.2586	0.2948
	SSIM	0.9819	0.9727	0.9644	0.9497	0.9381
NLR-SPIRiT	SNR	28.11	26.11	24.31	22.27	20.73
	HFEN	0.1223	0.1544	0.1909	0.2446	0.2849
	SSIM	0.9836	0.9761	0.9673	0.9529	0.9406

TABLE IV

COMPARISON OF THE THREE METRICS OF THE RECONSTRUCTED IMAGES, AS SHOWN IN FIG. 6. MSSIM IS CALCULATED ACCORDING TO THE METHOD IN [28].

Algorithms	SNR	HFEN	SSIM
JTV-SPIRiT [26]	23.26	0.0688	0.9901
LPJTV-ESPIRiT [19]	23.77	0.0578	0.9906
STDLR-SPIRiT [28]	24.46	0.0665	0.9919
NLR-SPIRiT-baseline	24.58	0.0608	0.9925
NLR-SPIRiT	25.51	0.0536	0.9935

approximately reaches the maximum SNR and the minimum HFEN when RE falls below $1e-4$. At this time, NLR-SPIRiT converges and then is terminated when RE falls below $1e-4$.

D. Comparison to previous works

In the following experiments, JTV-SPIRiT [26], LPJTV-ESPIRiT [19], STDLR-SPIRiT [28], NLR-SPIRiT-baseline, and NLR-SPIRiT were compared.

1) *Comparison results of 2DPU patterns*: To facilitate the assessment of the image quality (commonly a subjective parameter), Figs. 3-5 show the images reconstructed via all considered algorithms based on the 2DPU patterns ($AF = 5$), and their corresponding error maps. Fig. 3 shows that the reconstructed images via JTV-SPIRiT obvious artifacts. LPJTV-ESPIRiT, STDLR-SPIRiT and NLR-SPIRiT-baseline mitigate these artifacts to a certain extent. The proposed NLR-SPIRiT algorithm effectively removes image artifacts and preserves the details. Hence, NLR-SPIRiT achieves the best visual quality among all competing algorithms. Fig. 4 shows that the reconstructed images via JTV-SPIRiT and NLR-SPIRiT-baseline exhibit apparent artifacts. LPJTV-ESPIRiT and STDLR-SPIRiT mitigate artifacts to a certain extent. The proposed NLR-SPIRiT algorithm further removes these artifacts and succeeds in reconstructing certain details accurately, such as knee joint, whereas artifact areas remain in images more obviously reconstructed via other considered algorithms. NLR-SPIRiT produces the visually best reconstructed image

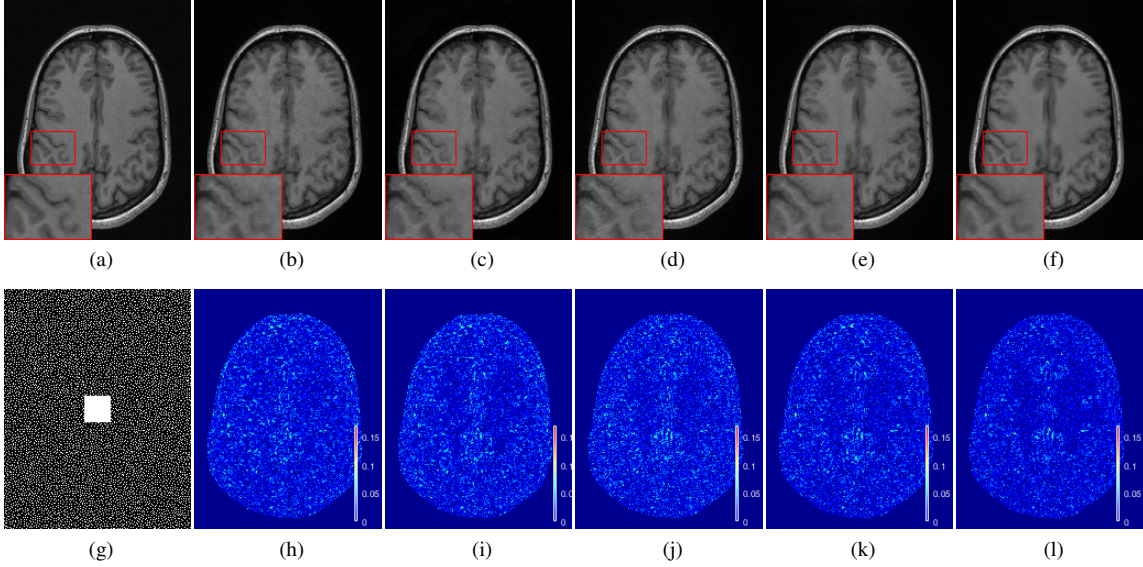


Fig. 3. Reconstructed results of dataset 1 based on the 2DPU pattern ($AF = 5$). (a) Reference image; (b) reconstructed image via JTV-SPIRiT [26]; (c) reconstructed image via LPJTV-ESPIRiT [19]; (d) reconstructed image via STDLR-SPIRiT [28]; (e) reconstructed image via the NLR-SPIRiT-baseline; (f) reconstructed image by NLR-SPIRiT; (g) undersampling pattern; (h), (i), (j), (k), and (l) show the error maps of (b), (c), (d), (e), and (f), respectively.

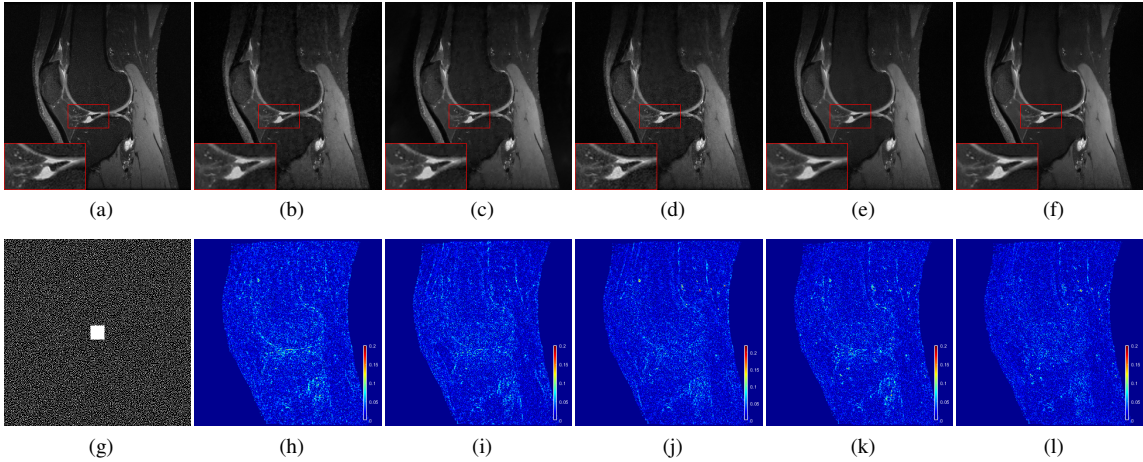


Fig. 4. Reconstructed results of dataset 2 based on the 2DPU pattern ($AF = 5$). (a) Reference image; (b) reconstructed image via JTV-SPIRiT [26]; (c) reconstructed image via LPJTV-ESPIRiT [19]; (d) reconstructed image via STDLR-SPIRiT [28]; (e) reconstructed image via the NLR-SPIRiT-baseline; (f) reconstructed image by NLR-SPIRiT; (g) undersampling pattern; (h), (i), (j), (k), and (l) show the error maps of (b), (c), (d), (e), and (f), respectively.

based on visual comparison. Fig. 5 shows that the reconstructed images via JTV-SPIRiT and STDLR-SPIRiT exhibit apparent artifacts. NLR-SPIRiT-baseline and STDLR-SPIRiT mitigate these artifacts effectively. NLR-SPIRiT obtain fewest errors and produces the visually best reconstructed image based on visual comparison. In summary, the proposed NLR-SPIRiT model achieves the best visual performance.

To quantitatively evaluate the reconstruction performance of all considered algorithms based on 2DPU patterns with different AF values, comparison results of the SNR, HFEN, and SSIM values of the reconstructed images via the considered algorithms are summarized in Tables I-III. The best metric in each case is marked in bold.

As indicated in Tables I-III, one can see that the proposed NLR-SPIRiT method produces the best metrics for all datasets and AF s. For dataset 1, NLR-SPIRiT achieves SNR improvements of 1.34, 1.41, 1.39, and 0.71 dB on average over JTV-

SPIRiT, LPJTV-ESPIRiT, STDLR-SPIRiT, and NLR-SPIRiT-baseline, respectively. In regard to dataset 2, NLR-SPIRiT achieves SNR improvements of 1.50, 1.01, 1.42, and 0.68 dB, respectively, on average. Regarding dataset 3, NLR-SPIRiT achieves SNR improvements of 1.40, 0.93, 1.09, and 0.48 dB, respectively, on average.

NLR-SPIRiT-baseline attains a better reconstruction performance than that of JTV-SPIRiT, LPJTV-ESPIRiT, and STDLR-SPIRiT except for a case (dataset 2 with $AF = 3$). In other words, the introduction of the NLR regularization term contributes to reconstruction performance improvement of these SPIRiT-based algorithms. Furthermore, NLR-SPIRiT improve the reconstruction performance than NLR-SPIRiT-baseline. NLR-SPIRiT achieves a significant improvement over JTV-SPIRiT, LPJTV-ESPIRiT, and STDLR-SPIRiT in terms of the three metrics.

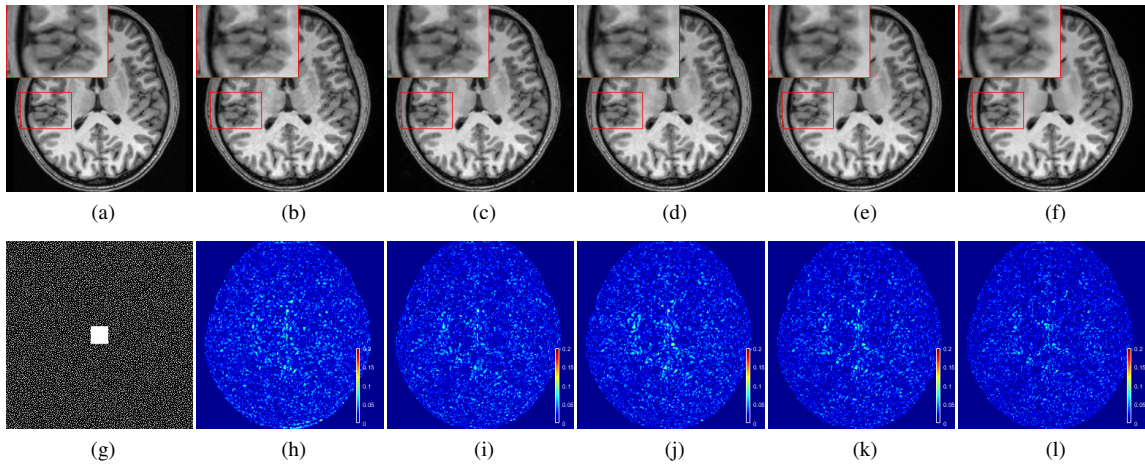


Fig. 5. Reconstructed results of dataset 3 based on the 2DPU pattern ($AF = 5$). (a) Reference image; (b) reconstructed image via JTV-SPIRiT [26]; (c) reconstructed image via LPJTV-ESPIRiT [19]; (d) reconstructed image via STDLR-SPIRiT [28]; (e) reconstructed image via the NLR-SPIRiT-baseline; (f) reconstructed image by NLR-SPIRiT; (g) undersampling pattern; (h), (i), (j), (k), and (l) show the error maps of (b), (c), (d), (e), and (f), respectively.

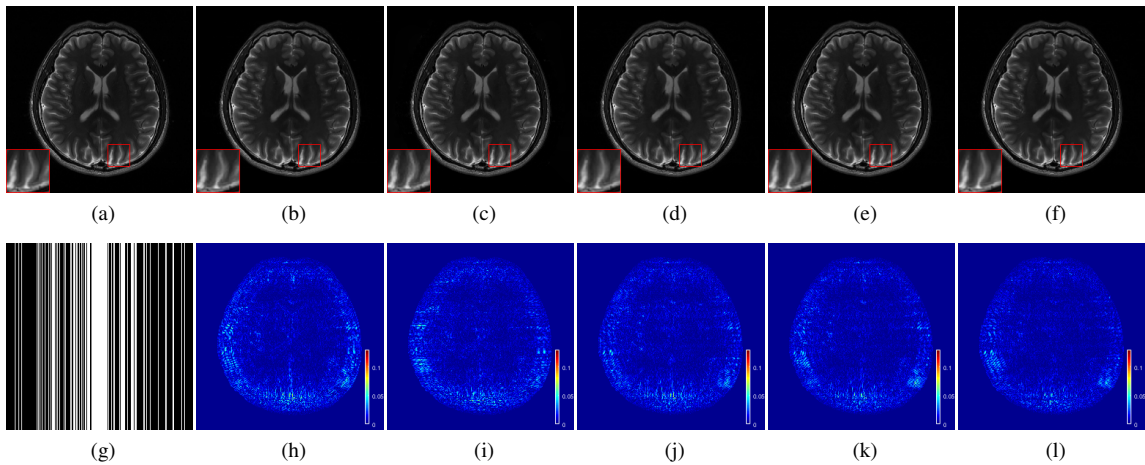


Fig. 6. Reconstructed results of dataset 4 based on the 1DGU pattern with a sampling rate of 0.34. (a) Reference image; (b) reconstructed image via JTV-SPIRiT [26]; (c) reconstructed image via LPJTV-ESPIRiT [19]; (d) reconstructed image via STDLR-SPIRiT [28]; (e) reconstructed image via the NLR-SPIRiT-baseline; (f) reconstructed image by NLR-SPIRiT; (g) undersampling pattern; (h), (i), (j), (k), and (l) show the error maps of (b), (c), (d), (e), and (f), respectively.

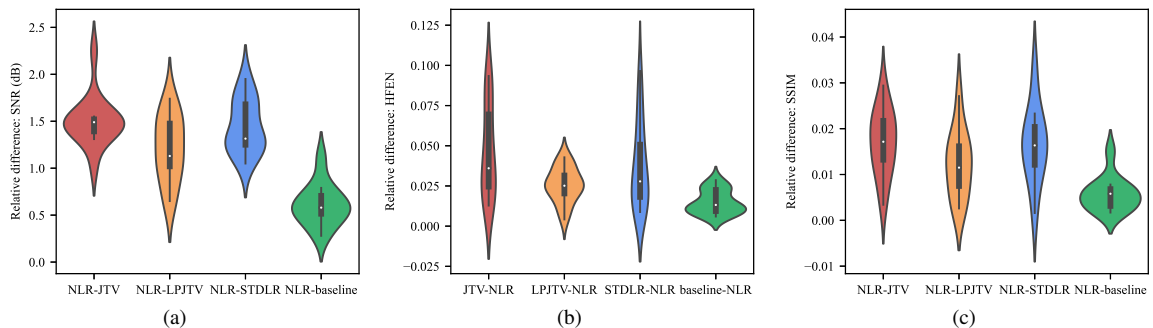


Fig. 7. Violin plots show the relative differences of (a) SNR, (b) HFEN, and (c) SSIM between NLR-SPIRiT and JTV-SPIRiT, LPJTV-ESPIRiT, STDLR-SPIRiT, and NLR-SPIRiT-baseline, which are simplified as NLR, JTV, LPJTV, STDLR, and baseline in plots, respectively.

2) *Comparison results of 1DGU patterns:* We choose the same data (dataset 4) and sampling pattern (1DGU pattern at a sampling rate of 0.34, which derived from Fig. 7(f) in 22) for comparison with the STDLR-SPIRiT [28] algorithm. The comparison of the PMRI reconstruction performance for dataset 4 under the 1DGU pattern is shown in Fig. 6(f).

As shown in Fig. 6, all the considered algorithms can produce a good reconstruction. And NLR-SPIRiT achieves the least artifacts inside the image and the least errors at the edge. It is shown that the proposed NLR-SPIRiT algorithm yields the highest visual quality among all considered algorithms.

Table IV summarizes the SNR, HFEN, and SSIM values of

TABLE V
COMPARISON OF THE RUNTIME AND MEMORY DEMANDS OF THE
CONSIDERED PMRI RECONSTRUCTION ALGORITHM FOR THE DATASET 1
BASED ON THE 2DPU PATTERN ($AF = 5$).

Algorithms	runime (s)	memory demand (GB)
JTV-SPIRiT [26]	28	0.46
LPJTV-ESPIRiT [19]	91	0.18
STDLR-SPIRiT [28]	1273	45.35
NLR-SPIRiT	796	0.49

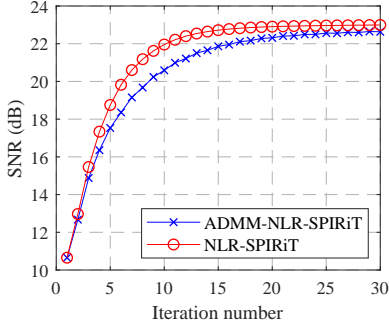


Fig. 8. SNR curves of ADMM-NLR-SPIRiT and NLR-SPIRiT for dataset 1 based on the 2DPU pattern ($AF = 5$).

the reconstructed images shown in Fig. 6. The results reveal that NLR-SPIRiT outperforms all considered algorithms under the 1DGU pattern in terms of these three metrics, consistent with the above visual comparison.

3) *Statistical analysis*: We also provide violin plots for the relative metric differences between NLR-SPIRiT and the compared algorithms in Table I-IV. As shown in Fig. 7, NLR-SPIRiT significantly outperforms JTV-SPIRiT, LPJTV-ESPIRiT, and STDLR-SPIRiT in terms of SNR, HFEN, and SSIM. In addition, we can also see that NLR-SPIRiT has slightly better performance than NLR-SPIRiT-baseline.

4) *Comparison of runtime and memory demand*: Next, we compare the runtime and memory demands of JTV-SPIRiT, LPJTV-ESPIRiT, STDLR-SPIRiT, and NLR-SPIRiT. Table V summarizes the runtime and memory demands of the considered algorithms in PMRI reconstruction for dataset 1 based on the 2DPU pattern ($AF = 5$). As indicated in Table V, JTV-SPIRiT has advantages in runtime and memory demands. Compared to JTV-SPIRiT, LPJTV-ESPIRiT consumes fewer memory but requires more runtime. STDLR-SPIRiT is the most advanced SPIRiT-based method at hand, which has the highest computational complexity, requires the longest runtime, and the maximum memory. Furthermore, NLR-SPIRiT requires 0.49 GB of RAM memory for reconstruction, only approximately one-92th of the memory demand of STDLR-SPIRiT. In other words, NLR-SPIRiT outperforms STDLR-SPIRiT in terms of memory demand and runtime.

The runtime of NLR-SPIRiT is $K \times (t_{BM}/T + t_{NLR} + t_1) + t_0$, where K is the outer iteration number, t_{BM} is the runtime of the block-matching operation performed every T iterations, t_{NLR} is the runtime of one LR approximation, t_1 is the runtime to update Z , X and u_Z once, and t_0 is the runtime of algorithm initialization and preprocessing. The very high computational complexity of the LR approximation and

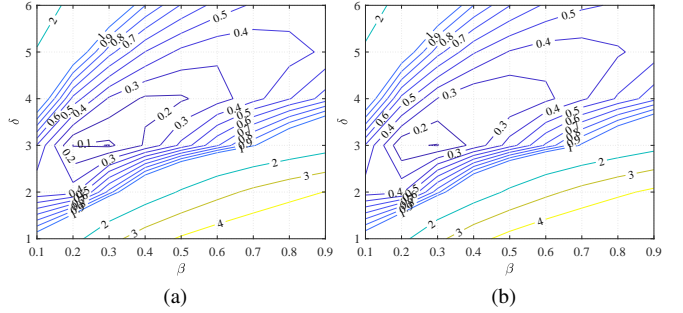


Fig. 9. We ran NLR-SPIRiT on the 15 training and 32 validation undersampling data sets on the ranges of $\delta \in [1, 6]$ and $\beta \in [0.1, 1]$, and obtained the average SNR relative differences between the maximum SNR and the SNR for each parameter setting. Contour plots show the average SNR relative differences of (a) 15 training data sets and (b) 32 validation data sets. The average SNR relative differences are also minimized around $\delta = 3$ and $\beta = 0.3$.

block-matching steps result in large t_{NLR} and t_{BM} values. Therefore, we will optimize the LR approximation step and block-matching steps with a graphics processing unit (GPU) to efficiently accelerate the proposed NLR-SPIRiT algorithm in the future.

E. Proposed NE formulation versus ADMM formulation

According to the derivations of the NLR-SPIRiT model and ADMM-NLR-SPIRiT algorithm (see the appendix), we observe that these two algorithms attain almost the same calculation time for one-iteration.

We compared the reconstruction results obtained with NLR-SPIRiT and ADMM-NLR-SPIRiT for dataset 1 based on the 2DPU pattern ($AF = 5$). As shown in Fig. 8, NLR-SPIRiT attains faster convergence and obtains a slightly higher SNR value than ADMM-NLR-SPIRiT. And we determine that they require almost the same reconstruction time every iteration. In addition, NLR-SPIRiT contains two fewer parameters than does ADMM-NLR-SPIRiT, and therefore it is easier to tune the parameters of NLR-SPIRiT. In summary, it is concluded that the proposed NLR-SPIRiT algorithm exhibits obvious advantages in practical applications.

F. Further discussion about parameter settings

We found that there exist similar parameters for reconstructing the MR images of same kind, so we also offer a parameter selection method for practical application. First, we train the parameters from 15 retrospective undersampling data sets with the 2DPU pattern ($AF = 5$). We ran NLR-SPIRiT on the training undersampling data sets on the ranges of $\delta \in [1, 6]$ and $\beta \in [0.1, 1]$, and obtained SNRs for different parameter settings. The average SNR relative difference between the maximum SNR and the SNR for each parameter setting is calculated. As shown in Fig. 9(a), the average SNR relative differences are minimized at $\delta = 3$ and $\beta = 0.3$. Second, we ran NLR-SPIRiT on the 32 retrospective validation undersampling data sets on the ranges of $\delta \in [1, 6]$ and $\beta \in [0.1, 1]$, and obtained the average SNR relative differences for each parameter setting. As shown in Fig. 9(b), the average SNR

relative differences are also minimized around $\delta = 3$ and $\beta = 0.3$. Therefore, for this kind of data sets, the optimal parameter setting was determined to be $\delta = 3$ and $\beta = 0.3$.

V. CONCLUSIONS

In this paper, we propose the NLR-SPIRiT model, which incorporates the NLR regularization into the SPIRiT model. The NLR-SPIRiT model fully utilizes both the NSS in MR images and the calibration consistency in the k-space domain. We adopt the WNN instead of the NN as a surrogate of the rank, and employ the NE formulation and the ADMM technique to efficiently solve the NLR-SPIRiT model. Experimental results considering four vivo datasets indicate that the proposed NLR-SPIRiT algorithm almost achieves a superior performance in terms of three objective metrics and visual perception over state-of-the-art methods. In addition, we propose a parameter setting method for practical application, which selects a set of near-optimal parameters for the same kind of MR images. We will optimize the most time-consuming BM and LR approximation steps with a GPU to efficiently accelerate the NLR-SPIRiT algorithm in the future. The proposed NLR-SPIRiT algorithm is very promising in regard to PMRI applications.

ACKNOWLEDGMENT

The authors would like to acknowledge Michael Lustig, Daniel S. Weller, Xinlin Zhang, Kevin Epperson, Fa-Hsuan Lin, Robreto Souza, Saiprasad Ravishankar, Bihan Wen, and Weisheng Dong, for making their code or in vivo data sets publicly available. The authors would like to thank the anonymous reviewers for their comments and suggestions.

APPENDIX

The PMRI reconstruction problem based on the NLR regularization and the SPIRiT model can be rewritten as follows:

$$X = \arg \min_X \frac{1}{2} \|AX - Y\|_F^2 + \frac{\mu_1}{2} \|(G - I)X\|_F^2 + \tau \sum_{c=1}^C \sum_{i=1}^{N_p} \text{rank}(V_{ci}(X)) \quad (28)$$

Problem (28) can be solved with the variable splitting (VS) and ADMM techniques. First of all, by introducing auxiliary variables $Z = X$, $D_{ci} = V_{ci}(X)$, $B = X$ and $D = [D_{11}, \dots, D_{ci}, \dots, D_{CN_p}]$, in addition to corresponding Lagrange multipliers u_Z , $u_{D_{ci}}$, u_B , and $u_D = [u_{D_{11}}, \dots, u_{D_{ci}}, \dots, u_{D_{CN_p}}]$, respectively, problem (28) is decomposed into the following subproblems via the ADMM method:

$$Z^{k+1} = \arg \min_Z \mu_1 \|(G - I)Z\|_F^2 + \beta_1 \|Z - (X^k + u_Z^k)\|_F^2 \quad (29)$$

$$\{D_{ci}^{k+1}\} = \arg \min_{\{D_{ci}\}} \frac{\beta_2}{2} \|D_{ci} - (V_{ci}(X^k) + u_{D_{ci}}^k)\|_F^2 + \tau \text{rank}(D_{ci}) \quad (30)$$

$$B^{k+1} = \arg \min_B \beta_2 \sum_{c=1}^C \sum_{i=1}^{N_p} \|V_{ci}(B) - (D_{ci}^{k+1} - u_{D_{ci}}^k)\|_F^2 + \beta_3 \|B - X^k - u_B^k\|_F^2 \quad (31)$$

$$X^{k+1} = \arg \min_X \|AX - Y\|_F^2 + \beta_1 \|X - (Z^{k+1} - u_Z^k)\|_F^2 + \beta_3 \|X - (B^{k+1} - u_B^k)\|_F^2 \quad (32)$$

$$u_Z^{k+1} = u_Z^k + \eta_1 (X^{k+1} - Z^{k+1}) \quad (33)$$

$$u_{D_{ci}}^{k+1} = u_{D_{ci}}^k + \eta_2 (V_{ci}(X^{k+1}) - D_{ci}^{k+1}) \quad (34)$$

$$u_B^{k+1} = u_B^k + \eta_3 (X^{k+1} - B^{k+1}) \quad (35)$$

As mentioned in Section III of the manuscript, the subproblems (29) and (30) are efficiently solved with respect to Z and D_{ci} , respectively. Subproblem (31) with respect to B yields the following closed-form solution:

$$B^{k+1} = \frac{\beta_2 \sum_{c=1}^C \sum_{i=1}^{N_p} V_{ci}^* (D_{ci}^{k+1} - u_{D_{ci}}^k) + \beta_3 (X^k + u_B^k)}{\beta_2 \sum_{c=1}^C \sum_{i=1}^{N_p} V_{ci}^* V_{ci} + \beta_3 I} \quad (36)$$

Subproblem (32) with respect to X generates a closed-form solution, which is expressed as follows:

$$X^{k+1} = \mathcal{F}^H \left[\frac{\mathcal{P}^H Y + \mathcal{F} (\beta_1 (Z^{k+1} - u_Z^k) + \beta_3 (B^{k+1} - u_B^k))}{\mathcal{P}^H \mathcal{P} + \beta_1 I + \beta_3 I} \right] \quad (37)$$

Now that subproblems (29)-(35) can be solved, we obtain the SPIRiT PMRI reconstruction algorithm, denoted as ADMM-NLR-SPIRiT.

REFERENCES

- [1] E. J. Candes, J. Romberg, T. Tao, Robust uncertainty principles: exact signal reconstruction from highly incomplete frequency information, *IEEE Transactions on Information Theory* 52 (2) (2006) 489–509. doi:10.1109/tit.2005.862083.
- [2] M. Lustig, D. Donoho, J. M. Pauly, Sparse MRI: The application of compressed sensing for rapid MR imaging, *Magnetic Resonance in Medicine* 58 (6) (2007) 1182–1195. doi:10.1002/mrm.21391.
- [3] J. Yang, Y. Zhang, W. Yin, A fast alternating direction method for TVL1-L2 signal reconstruction from partial Fourier data, *IEEE Journal of Selected Topics in Signal Processing* 4 (2) (2010) 288–297. doi:10.1109/jstsp.2010.2042333.
- [4] X. Qu, B. Ning, Y. Hou, Y. Lin, S. Cai, Z. Chen, Undersampled MRI reconstruction with patch-based directional wavelets., *Magnetic Resonance Imaging* 30 (7) (2012) 964–977. doi:10.1016/j.mri.2012.02.019.
- [5] B. Ning, X. Qu, D. Guo, C. Hu, Z. Chen, Magnetic resonance image reconstruction using trained geometric directions in 2D redundant wavelets domain and non-convex optimization., *Magnetic Resonance Imaging* 31 (9) (2013) 1611–1622. doi:10.1016/j.mri.2013.07.010.
- [6] Z. Lai, X. Qu, Y. Liu, D. Guo, J. Ye, Z. Zhan, Z. Chen, Image reconstruction of compressed sensing MRI using graph-based redundant wavelet transform., *Medical Image Analysis* 27 (2016) 93–104. doi:10.1016/j.media.2015.05.012.
- [7] S. Ravishankar, Y. Bresler, MR image reconstruction from highly undersampled k-space data by dictionary learning, *IEEE Transactions on Medical Imaging* 30 (5) (2011) 1028–1041. doi:10.1109/tmi.2010.2090538.
- [8] S. Ravishankar, Y. Bresler, Efficient blind compressed sensing using sparsifying transforms with convergence guarantees and application to magnetic resonance imaging, *SIAM Journal on Imaging Sciences* 8 (4) (2015) 2519–2557. doi:10.1137/141002293.
- [9] B. Wen, Y. Bresler, S. Ravishankar, FRIST - flipping and rotation invariant sparsifying transform learning and applications, *Inverse Problems* 33 (7) (2015) 074007. doi:10.1088/1361-6420/aa6c6e.
- [10] Z. Zhan, J.-F. Cai, D. Guo, Y. Liu, Z. Chen, X. Qu, Fast multiclass dictionaries learning with geometrical directions in MRI reconstruction, *IEEE Transactions on Biomedical Engineering* 63 (9) (2016) 1850–1861. doi:10.1109/tbme.2015.2503756.

- [11] S. Ravishankar, R. Nadakuditi, J. Fessler, Efficient sum of outer products dictionary learning (SOUP-DIL) and its application to inverse problems, *IEEE Transactions on Computational Imaging* 3 (4) (2017) 694–709. doi:10.1109/tci.2017.2697206.
- [12] J. V. Manjón, P. Coupé, L. Martí-Bonmatí, D. L. Collins, M. Robles, Adaptive non-local means denoising of MR images with spatially varying noise levels, *Journal of Magnetic Resonance Imaging* 31 (1) (2010) 192–203. doi:10.1002/jmri.22003.
- [13] K. Dabov, A. Foi, V. Katkovnik, K. Egiazarian, Image denoising by sparse 3-D transform-domain collaborative filtering, *IEEE Transactions on Image Processing* 16 (8) (2007) 2080–2095. doi:10.1109/tip.2007.901238.
- [14] E. M. Eksioğlu, Decoupled algorithm for MRI reconstruction using nonlocal block matching model: BM3D-MRI, *Journal of Mathematical Imaging and Vision* 56 (3) (2016) 430–440. doi:10.1007/s10851-016-0647-7.
- [15] X. Qu, Y. Hou, F. Lam, D. Guo, J. Zhong, Z. Chen, Magnetic resonance image reconstruction from undersampled measurements using a patch-based nonlocal operator, *Medical Image Analysis* 18 (6) (2014) 843–856. doi:10.1016/j.media.2013.09.007.
- [16] W. Dong, G. Shi, X. Li, Y. Ma, F. Huang, Compressive sensing via non-local low-rank regularization, *IEEE Transactions on Image Processing* 23 (8) (2014) 3618–3632. doi:10.1109/tip.2014.2329449.
- [17] K. P. Pruessmann, M. Weiger, M. B. Scheidegger, P. Boesiger, SENSE: sensitivity encoding for fast MRI, *Magnetic Resonance in Medicine* 42 (5) (1999) 952–962. doi:10.1002/(sici)1522-2594(199911)42:5<952::aid-mrm16\$>\$3.0.co;2-s.
- [18] M. Uecker, P. Lai, M. J. Murphy, P. Virtue, M. Elad, J. M. Pauly, S. S. Vasanawala, M. Lustig, ESPIRiT—an eigenvalue approach to autocalibrating parallel MRI: Where SENSE meets GRAPPA, *Magnetic Resonance in Medicine* 71 (3) (2014) 990–1001. doi:10.1002/mrm.24751.
- [19] J. Duan, Z. Bao, Y. Liu, Eigenvector-based SPIRiT parallel MR imaging reconstruction based on L_p pseudo-norm joint total variation, *Magnetic Resonance Imaging* 58 (2019) 108–115. doi:10.1016/j.mri.2019.01.014.
- [20] M. A. Griswold, P. M. Jakob, R. M. Heidemann, M. Nittka, V. Jellus, J. Wang, B. Kiefer, A. Haase, Generalized autocalibrating partially parallel acquisitions (GRAPPA), *Magnetic Resonance in Medicine* 47 (6) (2002) 1202–1210. doi:10.1002/mrm.10171.
- [21] Y. Chang, D. Liang, L. Ying, Nonlinear GRAPPA: A kernel approach to parallel MRI reconstruction, *Magnetic Resonance in Medicine* 68 (3) (2012) 730–740. doi:10.1002/mrm.23279.
- [22] M. Lustig, M. Alley, S. Vasanawala, D. Donoho, J. Pauly, L_1 SPIRiT: Autocalibrating parallel imaging compressed sensing, in: *International Society for Magnetic Resonance in Medicine (ISMRM)*, Honolulu, Hawaii, 2009, p. 334.
- [23] M. Lustig, J. M. Pauly, SPIRiT: Iterative self-consistent parallel imaging reconstruction from arbitrary k -space, *Magnetic Resonance in Medicine* 64 (2) (2010) 457–471. doi:10.1002/mrm.22428.
- [24] M. Murphy, M. Alley, J. Demmel, K. Keutzer, S. Vasanawala, M. Lustig, Fast L_1 -SPIRiT compressed sensing parallel imaging MRI: Scalable parallel implementation and clinically feasible runtime, *IEEE Transactions on Medical Imaging* 31 (6) (2012) 1250–1262. doi:10.1109/TMI.2012.2188039.
- [25] J. Duan, L. Zhang, Y. Liu, Y. Sun, Efficient reconstruction algorithm for parallel magnetic resonance imaging based on self-consistency, *Journal of Tianjin University* 47 (5) (2014) 414–419. doi:10.11784/tdxbz201208036.
- [26] D. S. Weller, S. Ramani, J. A. Fessler, Augmented Lagrangian with variable splitting for faster non-Cartesian L_1 -SPIRiT MR image reconstruction, *IEEE Transactions on Medical Imaging* 33 (2) (2014) 351–361. doi:10.1109/TMI.2013.2285046.
- [27] J. Duan, Y. Liu, P. Jing, Efficient operator splitting algorithm for joint sparsity-regularized SPIRiT-based parallel MR imaging reconstruction, *Magnetic Resonance Imaging* 46 (2018) 81–89. doi:10.1016/j.mri.2017.10.013.
- [28] X. Zhang, D. Guo, Y. Huang, Y. Chen, L. Wang, F. Huang, Q. Xu, X. Qu, Image reconstruction with low-rankness and self-consistency of k -space data in parallel MRI, *Medical Image Analysis* 63 (2020) 101687. doi:10.1088/1361-6560/abd4b8.
- [29] B. Wen, Y. Li, Y. Bresler, Image recovery via transform learning and low-rank modeling: The power of complementary regularizers, *IEEE Transactions on Image Processing* 29 (2020) 5310–5323. doi:10.1109/tip.2020.2980753.
- [30] A. Danielyan, V. Katkovnik, K. Egiazarian, BM3D frames and variational image deblurring, *IEEE Trans Image Process* 21 (4) (2012) 1715–1728. doi:10.1109/tip.2011.2176954.
- [31] H. Yoon, K. S. Kim, D. Kim, Y. Bresler, J. C. Ye, Motion adaptive patch-based low-rank approach for compressed sensing cardiac cine MRI, *IEEE Transactions on Medical Imaging* 33 (11) (2014) 2069–2085. doi:10.1109/tmi.2014.2330426.
- [32] S. Gu, L. Zhang, W. Zuo, X. Feng, Weighted nuclear norm minimization with application to image denoising, in: *IEEE Conference on Computer Vision and Pattern Recognition (CVPR)*, Columbus, OH, USA, 2014, pp. 2862–2869. doi:10.1109/cvpr.2014.366.
- [33] C. Lu, J. Tang, S. Yan, Z. Lin, Nonconvex nonsmooth low rank minimization via iteratively reweighted nuclear norm, *IEEE Transactions on Image Processing* 25 (2) (2016) 829–839. doi:10.1109/tip.2015.2511584.
- [34] R. Souza, M. Bento, N. Nogovitsyn, K. Chung, W. Loos, R. Lebel, R. Frayne, Dual-domain cascade of U-nets for multi-channel magnetic resonance image reconstruction, *Magnetic Resonance Imaging* 71 (2020) 140–153. doi:10.1016/j.mri.2020.06.002.
- [35] K. Epperson, A. M. Sawyer, M. Lustig, M. Alley, M. Uecker, P. Virtue, P. Lai, M. D. Shreyas Vasanawala, Creation of fully sampled MR data repository for compressed sensing of the knee.
- [36] F.-H. Lin, mprage_8ch_slice1.mat, http://www.nmr.mgh.harvard.edu/~fhlin/codes/mprage_8ch_slice1.mat, accessed April 4, 2013.
- [37] Z. Wang, A. C. Bovik, H. R. Sheikh, E. P. Simoncelli, Image quality assessment: from error visibility to structural similarity, *IEEE Transactions on Image Processing* 13 (4) (2004) 600–612. doi:10.1109/tip.2003.819861.